**PAPER**

Check for updates

# *In situ* formation of 2-thiobarbituric acid incorporated g-C$_3$N$_4$ for enhanced visible-light-driven photocatalytic performance†

Tingting Chen,‡[a] Shan Hu,‡[ab] Quanfeng Xing,[a] Xiaofeng Yu,[c] Jinming Chen,[c] Xiaolong Li,[c] Xiuquan Xu [ID] *[c] and Bo Zhang[ab]

Embedding heterocycles into the skeleton of g-C$_3$N$_4$ has been proved to be a simple and efficient strategy for improving light response and the separation of photo-excited charges. Herein, 2-thiobarbituric acid incorporated g-C$_3$N$_4$ (TBA/CN) with good photocatalytic efficiency for Rh B degradation and H$_2$ production was successfully achieved *via* a facile thermal copolymerization approach. The incorporation of aromatics and S atoms into the skeleton of g-C$_3$N$_4$ was identified *via* systematic characterizations. This unique structure contributed to the narrowed band-gap, extended delocalization of lone pair electrons and changed electron transition pathway, which led to the enhanced visible light utilization, accelerated charge migration and prolonged electron lifetime, subsequently resulting in the significant boost of photocatalytic activity. The optimal TBA/CN-3 sample yielded the largest Rh B degradation rate constant $k$ value of 0.0273 min$^{-1}$ and simultaneously highest rate of H$_2$ evolution of 0.438 mmol g$^{-1}$ h$^{-1}$, which were almost 3.5 and 3.8 folds as fast as that of the pristine CN, respectively. Finally, the photocatalytic mechanism was proposed for the detailed elucidation of the process of Rh B degradation coupled with H$_2$ production.

## 1. Introduction

In recent decades, emerging global energy dilemma and environmental pollution have become the two urgent threats to human existence and social development.[1,2] Semiconductor photocatalysis has widely proven to be one of the most encouraging and prospective alternative techniques for effectively easing up the energy crisis and environmental issues due to its incorporated merits of high efficiency, energy-saving ability and eco-friendliness.[3–5] Numerous photocatalysts have been constructed and successfully employed for H$_2$ evolution, pollutant degradation and the conversion of CO$_2$ to CO and CH$_4$. However, the practical application of traditional photocatalysts, such as TiO$_2$ and WO$_3$, was mostly suppressed by the limitations of toxicity, high cost, low efficiency and insufficient visible light utilization.[6–8]

Recently, graphitic carbon nitride (g-C$_3$N$_4$, CN), a metal-free semiconductor polymer, has received unprecedented attention due to its unique traits of visible-light-driven, tunable electronic
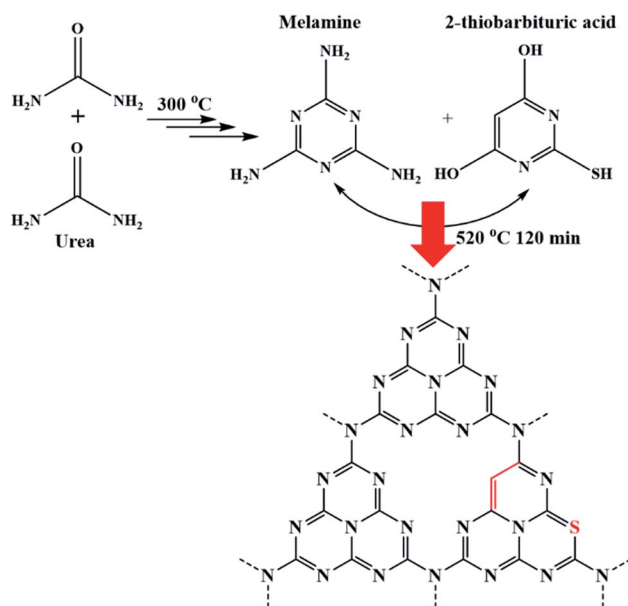


**Fig. 1** Presentation of the possible formation processes for 2-thiobarbituric acid modified g-C$_3$N$_4$.

[a]School of Environment and Safety Engineering, Jiangsu University, Zhenjiang 212013, PR China

[b]Jiangsu Province Synergistic Innovation Center of Modern Agricultural Equipment and Technology, Zhenjiang 212013, PR China

[c]School of Pharmacy, Jiangsu University, Zhenjiang 212013, PR China. E-mail: xxq781026@ujs.edu.cn

‡ These authors contributed equally to this work.

structure, physical–chemical stability, good-durability, inexpensive nature and facile synthesis, which are perfect fit for the $H_2$ production, pollutant degradation, and $CO_2$ reduction.[9–11] Nevertheless, the practical applicability of CN is still restricted by its inherent bottlenecks of limited visible light harvesting and ultrafast recombination rate of photogenerated charge carriers.[12,13] To overcome the above-mentioned defects, considerable efforts have been devoted to boost the photocatalytic property of CN, including porous morphology formation,[14] heteroatom doping,[15] heterostructure construction,[16] aromatic ring integration[17] and dye sensitization.[18]

Among these, embedding heteroaromatic molecules into the skeleton of CN has been confirmed to be an effective strategy, which resulted in an extended π-conjugated system and new localized internal field formation, could expand the visible light response range and facilitate the separation and transportation of charges, leading to an increased photocatalytic efficiency.[17,19,20] To date, numerous small molecules containing aromatic rings, such as tris(*p*-fluorophenyl)phosphine,[21] thiophene,[22] benzene,[23] pyridine[24] and salicylic acid,[25] have been copolymerized successfully into the framework of CN, which not only resulted in the facilitation of visible-light utilization and increasing charge separation efficiency, but also modulated
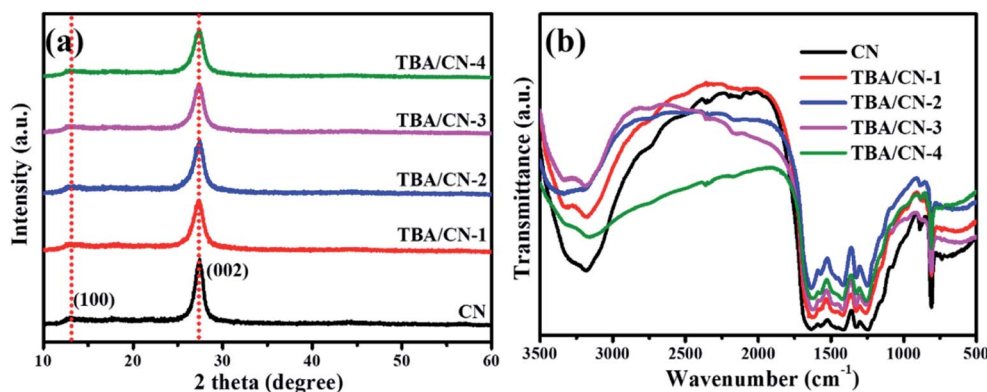


**Fig. 2** XRD patterns (a) and FT–IR spectra (b) for pristine CN, TBA/CN-1, TBA/CN-2, TBA/CN-3 and TBA/CN-4.
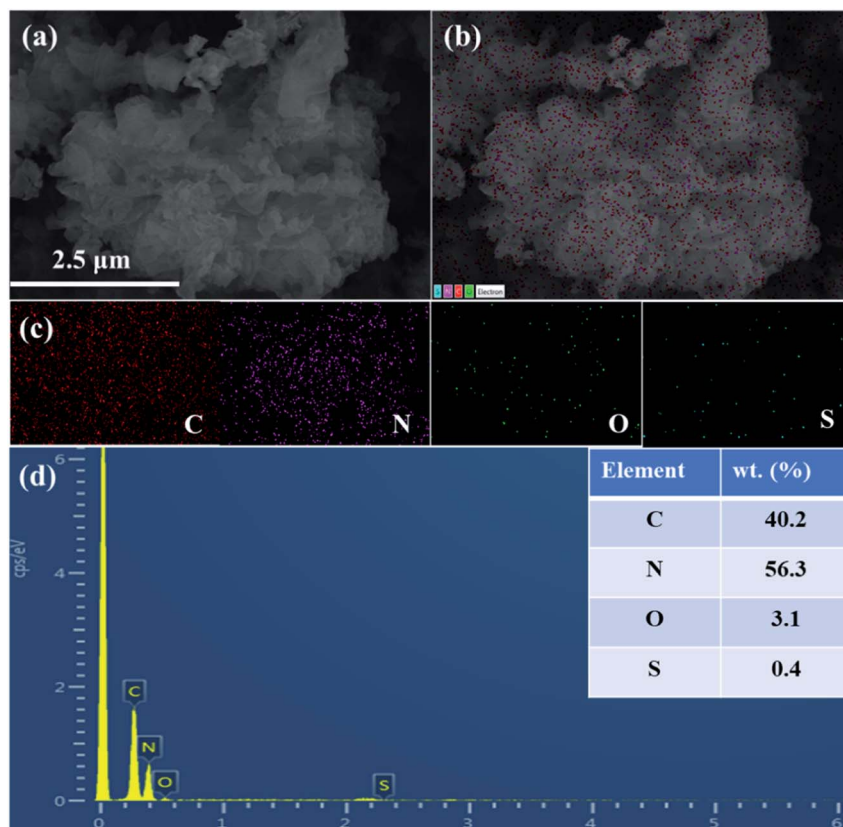


**Fig. 3** SEM image (a), the corresponding elemental maps (b and c) and EDS pattern (d) of TBA/CN-3.
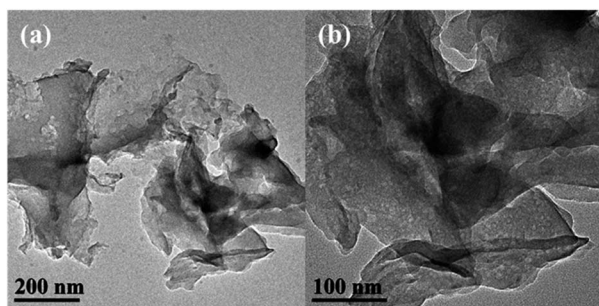
**Fig. 4** TEM images of TBA/CN-3.

the redox band potentials, making the effective use of photo-excited charge carriers.

Motivated by the above-mentioned discussion, in this study, 2-thiobarbituric acid incorporated CN was synthesized *via* a thermal copolymerization approach. Fascinatingly, the as-synthesized TBA/CN composites endowed improved visible-light utilization and accelerative separation efficiency of photo-excited charge carriers, resulting in a substantially boosted photocatalytic performance towards the degradation of Rh B and $H_2$ evolution. Furthermore, the possible mechanism for the outstanding improved photocatalytic property was deeply interpreted.

## 2. Experimental section

### 2.1. Photocatalyst preparation and characterization

Analytical pure grade urea and 2-thiobarbituric acid purchased from Aladdin Chemical Reagent Co., Ltd (Shanghai, China) were used as precursors. The modified CN composites were synthesized *via* a direct annealing route. In detail, the mixture of 20 g urea and desired amounts (0.05, 0.1, 0.2 and 0.3 g) of 2-thiobarbituric acid was completely dissolved in 5 mL ultrapure water *via* magnetic stirring. After drying at 60 °C overnight, the obtained residues were placed into a covered crucible and heated at 520 °C for 120 min at an increasing rate of 5 °C min⁻¹. When restoring to room temperature, the resulting composites were collected and labeled as TBA/CN-1, TBA/CN-2, TBA/CN-3 and TBA/CN-4 correspondingly.

For comparison, pristine g-$C_3N_4$ was also obtained *via* the direct calcination of urea under the same procedure, and the final product was named as CN.

The crystal and molecular structures, the surface morphologies and elemental composition and the light response behaviors of the as-synthesized composites were systematically characterized *via* X-ray diffraction (XRD), Fourier transformed infrared (FT-IR) spectroscopy, scanning electron microscopy (SEM), transmission electron microscopy (TEM), UV-Vis diffuse reflectance spectroscopy (UV-Vis DRS), X-ray photoelectron spectroscopy (XPS), photoluminescence (PL) spectroscopy and time-resolved photoluminescence (TRPL) spectroscopy.

The photoelectrochemical behaviors of these samples, including photocurrent (PC) response and electrochemical impedance spectra (EIS), were recorded on a CHI 760E electrochemical workstation.

### 2.2. Photocatalytic performance measurements

The visible-light driven photocatalytic properties of the as-synthesized samples were assessed by Rh B degradation coupled with $H_2$ production. A 300 W Xe lamp ($\lambda > 420$ nm) was chosen as the radiation source and ultrapure water was employed throughout the experiments.

In a typical degradation experiment, 50 mg of the photocatalyst was fully mixed with 100 mL of Rh B (10 mg L⁻¹) by ultrasonic treatment for 5 min. Before exposure to light, the reaction system achieved adsorption–desorption equilibrium by magnetic stirring for 30 min in darkness. At designated intervals, 3.0 mL suspension was collected and centrifuged at 12 000 rpm for 10 min. Finally, the concentration of Rh B in the supernatant was estimated using a Unico UV-2800A spectrophotometer at the characteristic wavelength of 552 nm.

In the photocatalytic $H_2$ generation test, 30 mg of sample deposited with 1.0 wt% Pt was fully suspended into 50 mL ultrapure water containing 10% (vol/vol) triethanolamine (TEOA), where TEOA was used as the hole scavenger and Pt was used as the co-catalyst. $H_2$ evolution during the photocatalytic reaction was calculated using an online gas chromatograph (Agilent, GC-8890) equipped with a thermal conductivity detector and high-purity nitrogen was used as the carrier gas.
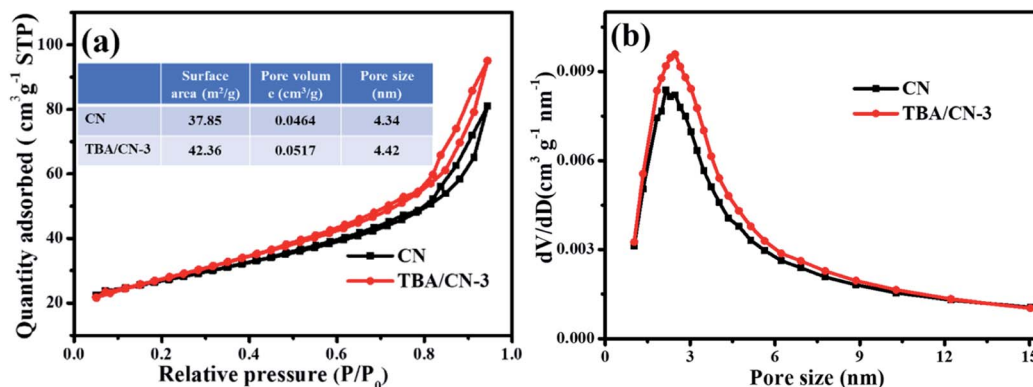


**Fig. 5** $N_2$ adsorption–desorption isotherms of CN, TBA/CN-3 (a) and the corresponding pore-size distribution curves (b).
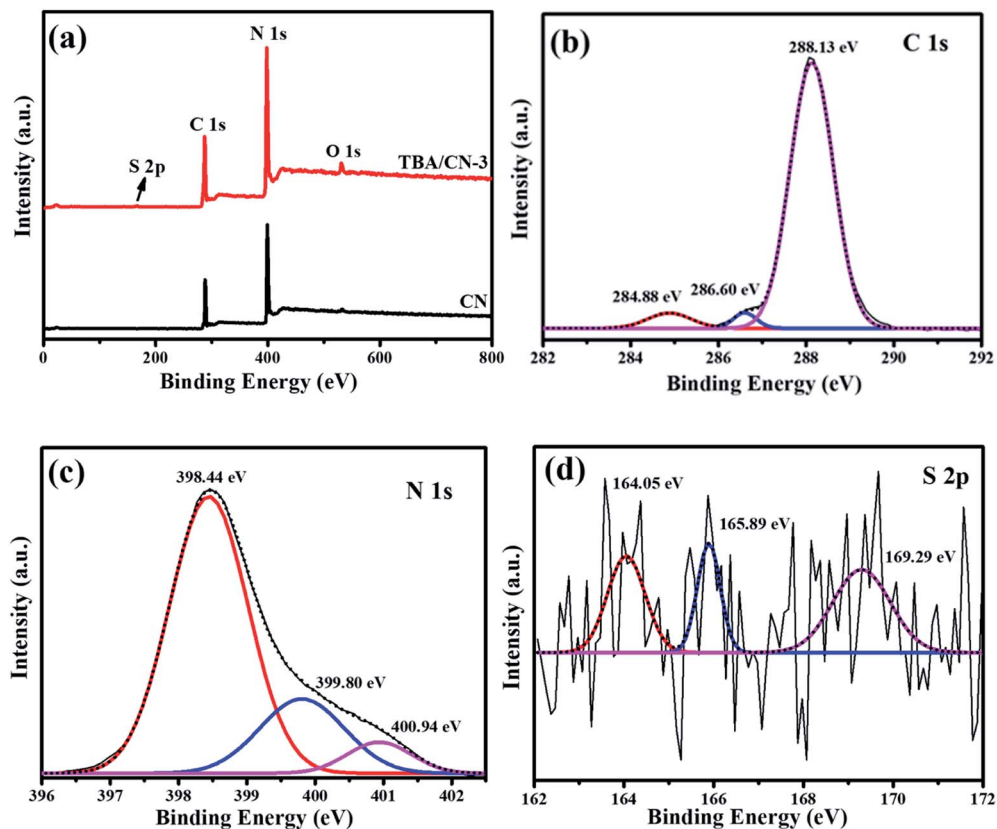
**Fig. 6** Survey XPS spectra (a) and high-resolution XPS spectra of C 1s (b), N 1s (c) and S 2p (d) for TBA/CN-3.
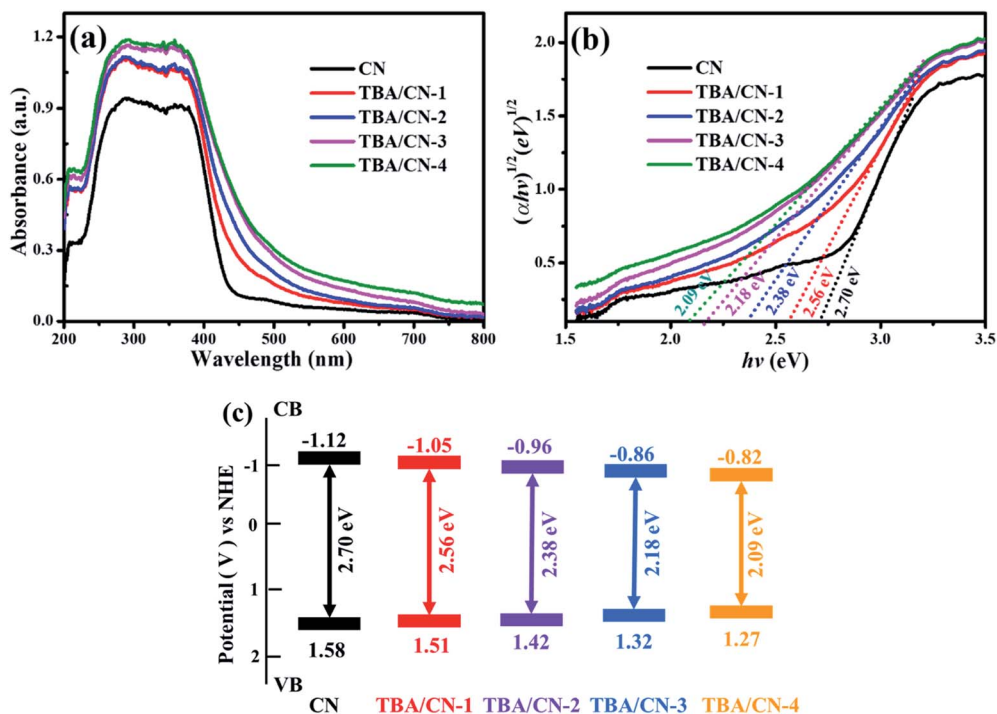


**Fig. 7** UV-Vis DRS (a), the plot of $(\alpha h v)^{1/2}$ *versus* the energy of light ($hv$) spectra (b) and the band edge potentials (c) of the as-prepared samples.

# 3. Results and discussion

### 3.1. Material characterization

The possible reaction route for the TBA/CN framework is shown in Fig. 1. Here, the crystal and molecular structures of the as-synthesized composites were first identified by the XRD and FT-IR analyses. As depicted in Fig. 2a, all the samples possessed two typical diffraction peaks of graphitic materials at around 12.9° and 27.5°, corresponding to the (100) and (002) crystal facets (JCPDS 87-1526),[26] which suggested that the original crystal structure of CN was largely intact after the introduction of small amounts of TBA. Specifically, the front peak was related to the in-plane repeating motifs of tri-s-triazine, while the subsequent peak was attributed to the repeated interfacial stacking of the conjugated aromatic system in the CN nanosheets, respectively.[27,28]

Moreover, the obtained TBA/CN samples exhibited essentially similar FT-IR feature to that of pristine CN. In detail, the wide band located in the region between 3000 and 3400 cm$^{-1}$ was derived from the terminal N–H and surface-adsorbed O–H stretching vibrations.[29] Series of characteristic signals in the fingerprint region from 1150 to 1700 cm$^{-1}$ were related to the different types of aromatic C–N or C–C stretching vibrations in the tri-s-triazine ring and heptazine heterocyclic ring units.[30,31]

Finally, the sharp peak at 809 cm$^{-1}$ was attributed to the unique breathing vibration of the heptazine units.[32] In addition, no evident absorption peaks associated with the bonds of the S atom were detected in the FT-IR spectra mainly due to its low modification level and relatively weak absorption.[33]

The morphology of TBA/CN-3 was observed by SEM and TEM. Fig. 3a indicated that TBA/CN-3 displayed an aggregated multilayer porous two-dimensional structure, which was in good accordance with the typical urea-derived CN structure.[34] The corresponding elemental mapping (Fig. 3b and c) clearly reveal that C, N, O, and S elements were evenly dispersed throughout the TBA/CN-3 samples, demonstrating that TBA was successfully integrated into the CN skeleton. This result could be further confirmed by EDS, exhibiting the presence of C, N, O and S in the TBA/CN-3 sample. The representative TEM image of TBA/CN-3, as given in Fig. 4, also elucidated the ultrathin nanosheet-like structure equipped with abundant nanosized pores, which was largely due to the gas templating effects of urea and TBA.[35] The ultrathin nanosheet morphology and enriched nanoholes on the surface of TBA/CN-3 would provide more active sites and might lead to significant acceleration of the photo-excited charge separation and migration, subsequently resulting in much improved photoactivity.[36,37]
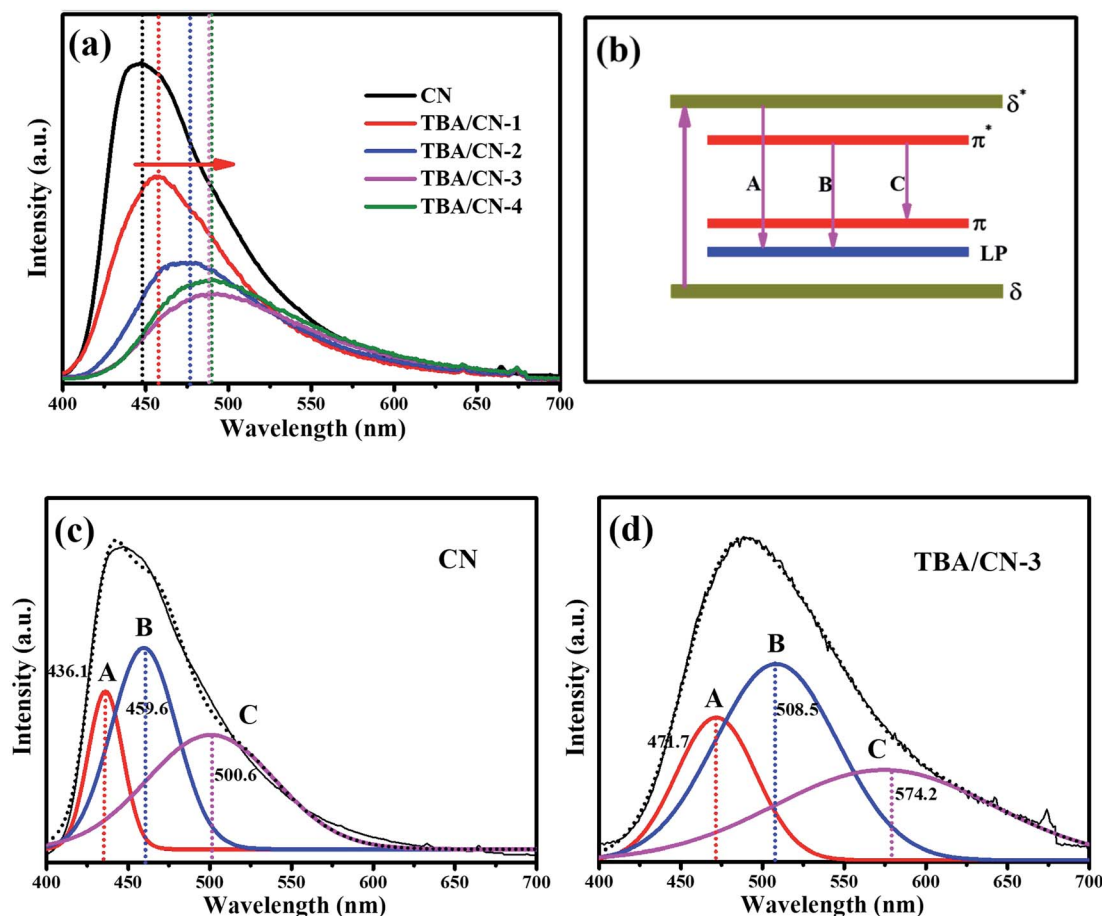


Fig. 8 PL spectra of the as-prepared samples (a). Schematic of the electron transition form of CN (b). The Gaussian fitting of the PL spectra of CN (c) and TBA/CN-3 (d).

The porous feature of TBA/CN-3 was further identified by $N_2$ adsorption–desorption isotherms. As depicted in Fig. 5a, the isotherms of TBA/CN-3 as well as CN exhibited typical type IV curves featured with H3 hysteresis loops, suggesting their unaltered mesoporous structures.[38] The BJH pore size distribution plots in Fig. 5b demonstrated that both TBA/CN-3 and pure CN had porous structures with average pore sizes of about 4.0 nm, which was quite consistent with the results of TEM. The almost similar parameters of BET specific surface area, pore volume and average pore size further confirmed that the structural integrity of CN remained intact even after the introduction of TBA. Thus, the enhancement of photocatalytic efficiency was mainly due to the incorporation of TBA rather than the surface morphology change of CN.

The XPS analysis was carried out to gain insight into the surface composition and valence states of different elements in CN and TBA/CN-3 samples, and the results are depicted in Fig. 6. From the XPS survey spectra (Fig. 6a), the peaks of C 1s, N 1s and O 1s could be clearly detected in both the samples, while the S 2p peak was only presented in the TBA/CN-3 sample. The weak absorption peaks of S 2p in the survey spectrum of TBA/CN-3 are mainly due to the small introduced content. The C 1s high-resolution XPS spectrum of TBA/CN-3 (Fig. 6b) could be well fitted into three peaks centered at 284.88, 286.60 and 288.13 eV, which correspond to the different chemical environments of carbon including C–C, C–

$NH_2$ and N–C$=$N in the heterocycle, respectively.[39,40] In addition, with respect to the C 1s high-resolution XPS spectrum of CN provided in Fig. S1b,† no difference between TBA/CN-3 and CN was detected, indicating the occurrence of little change in the basic skeleton structure of CN. Similarly, the N 1s high-resolution XPS spectrum of TBA/CN-3 (Fig. 6c) was also consistent with that of the pristine CN (Fig. S1c†). Specifically, the three peaks with bond energies of 398.44, 399.80 and 400.94 eV were assigned to C–N$=$C, $(C)_3$–N and terminal C–N–H amino functional groups, respectively.[41] In terms of the S 2p XPS spectrum (Fig. 6d), TBA/CN-3 presented three peaks at 164.05, 165.89 and 169.29 eV, corresponding to the C–S bond, S$=$C bond and oxidized S (S–$O_x$) generated during annealing.[42,43] The S atom with extra electrons introduced into the CN skeleton could lead to a significant electronic polarization effect, which would be highly conducive to the migration and conductivity of the charge carriers.[44]

The optical behaviors of the as-synthesized samples were evaluated by UV-Vis DRS and the corresponding band gaps were obtained according to the method of Kubelka–Munk.[45] As presented in Fig. 7, pristine CN had a fundamental absorption edge at about 440 nm, with the calculated value of band gap being 2.70 eV. In comparison, the TBA/CN samples displayed a noticeable gradual red-shift and stronger response in the visible light region with the increase in TBA.
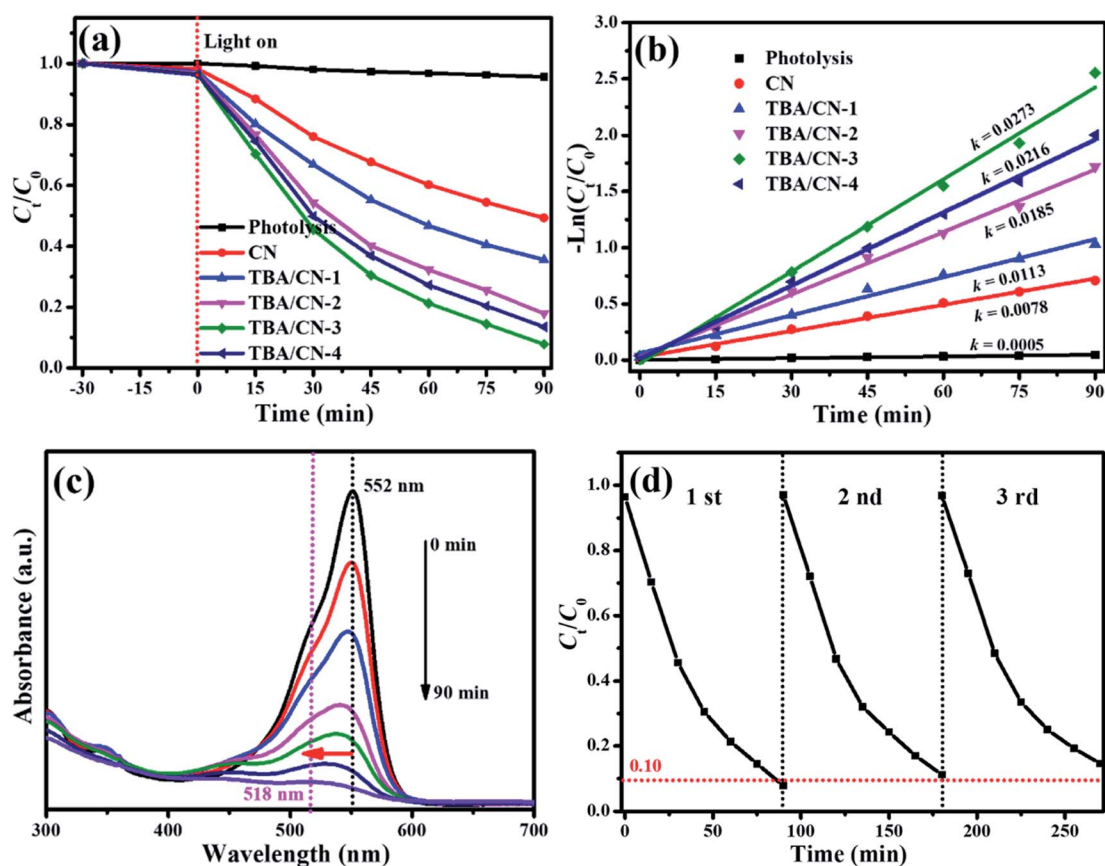


**Fig. 9** Photocatalytic degradation of Rh B (a), the first-order-kinetic plots of as-prepared samples (b), the UV–vis absorption spectral changes of Rh B (c) and the stability (d) over the TBA/CN-3 sample.

The electronic band structure of VB and CB for the as-synthesized samples could be calculated according to the following formula:[46]

$$E_{VB} = X - E_e + 1/2E_g$$

$$E_{CB} = E_{VB} - E_g$$

where $X$ is the semiconductor absolute electronegativity (CN = ~4.73 V $vs.$ NHE), $E_e$ is the free electron energy (~4.5 V $vs.$ NHE).

Therefore, the $E_{VB}$ values of CN and TBA/CN samples were calculated to be 1.58, 1.51, 1.42, 1.32 and 1.27 eV, while the $E_{CB}$ values were −1.12, −1.05, −0.96, −0.86 and −0.82 eV, respectively (Fig. 7c). Hence, it can be clearly deduced that the TBA modification could narrow the band gap of CN, which resulted in more visible light harvest, consequently elevating the generation of photo-excited charges and thus improving the photocatalytic properties.

The separation efficiency and migration behaviors of the photo-excited charges over CN and TBA/CN samples were compared $via$ the PL analysis. Fig. 8a presents the particular strong emission peak of pristine CN at 448 nm, suggesting the immense recombination of photo-excited charges.[47] Compared with CN, the peak intensities of TBA/CN samples significantly reduced and gradually redshifted to 456, 477, 490 and 492 nm for TBA/CN-1, TBA/CN-2, TBA/CN-3 and TBA/CN-4

correspondingly, which were consistent with the results of the UV-Vis DRS analysis. TBA/CN-3 possessed the weakest PL peak intensity, which indicated that the recombination of the photoinduced carriers was most effectively restrained.[48] As shown in Fig. 8b and c, based on Gaussian fitting, the PL emission of CN could be well deconvoluted into three peaks centered at 436.1, 459.6 and 500.6 nm, corresponding to the electron transition pathways of σ*–LP (lone pair state), π*–p, and π*–LP.[49,50] However, these three peaks of TBA/CN-3 clearly redshifted to 471.7, 508.5 and 574.2 nm in comparison to those of CN, suggesting that the electronic transition pathway has changed. Moreover, the improved ratio of peaks B and C of TBA/CN-3 revealed that the corresponding electronic transition types of π*–p, and π*–LP dominated, which was mainly due to the increase in the sp$^2$ C=C bonds and S atoms with more valence electrons by the incorporation of TBA.[51]

Therefore, these results implied that the loading of TBA with abundant aromatic C=C bonds and S heteroatoms could change the electron transition path, thus preventing the charge recombination, which would result in an enhancement of the photocatalytic performance.

### 3.2. Photocatalytic property

The photodecomposition of Rh B was first carried out to evaluate the photocatalytic activity of the as-synthesized samples. As
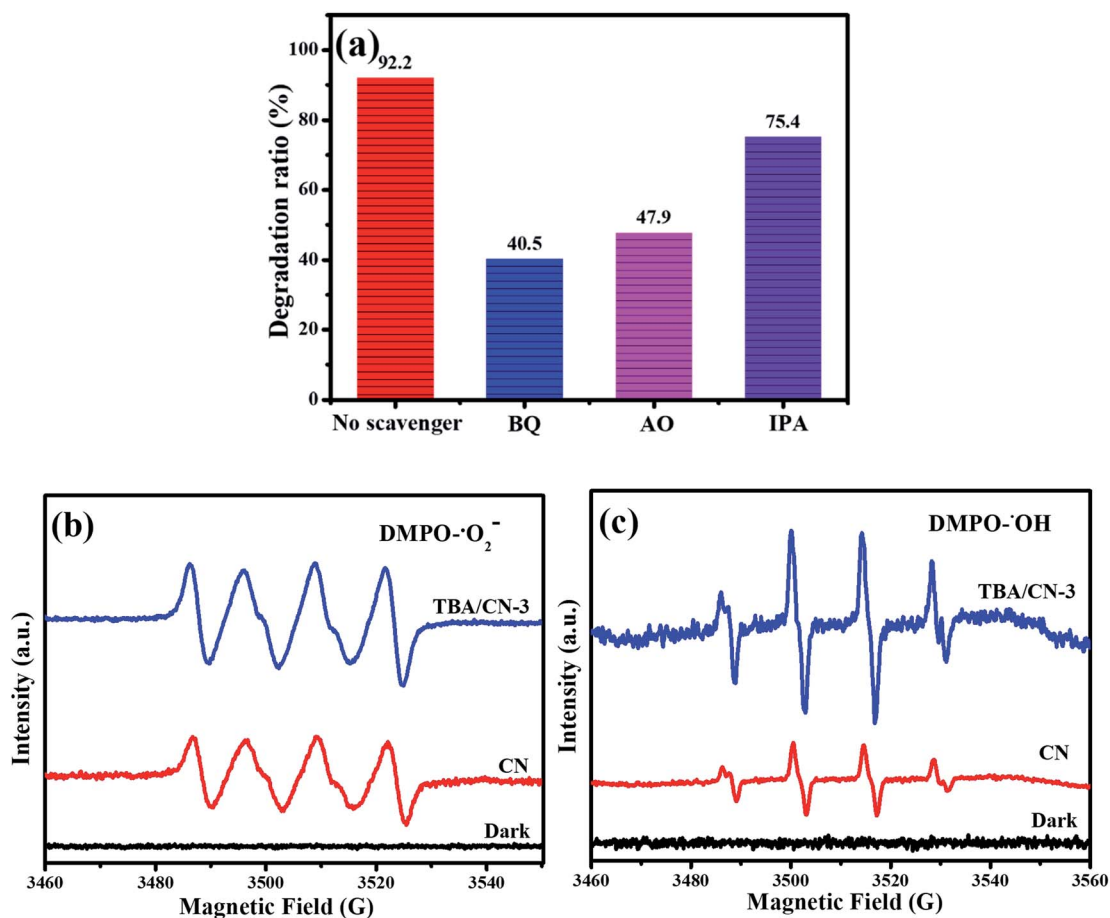


Fig. 10 Effect of different scavengers on the photodegradation of Rh B (a), ESR spectra of DMPO-˙O₂⁻ (b) and DMPO-˙OH (c) over TBA/CN-3.

presented in Fig. 9a, a negligible change of Rh B after 90 min visible light exposure demonstrated that it was very stable under the experimental conditions. After adding the photocatalyst, the degradation efficiency significantly enhanced, and the TBA/CN samples showed better degradation effect than the pristine CN. As expected, TBA/CN-3 showed the optimal photocatalytic efficiency and about 92.0% of Rh B could be removed after 90 min of visible light illumination. However, the TBA/CN-4 sample with the narrowest band gap of 2.09 eV exhibited reduced degradation activity, which can be possibly due to the formation of recombination centers and the reduction of charge separation efficiency caused by excessive TBA incorporation.[52] The corresponding degradation kinetics was calculated by the following pseudo-first-order equation: $-\ln\left(\dfrac{C}{C_0}\right) = kt$,[53] and the results are shown in Fig. 9b. The largest rate constant $k$ value of $0.0273$ min$^{-1}$ for TBA/CN-3 was obtained, which was almost 3.5-fold as that of the pristine CN. Fig. 9c depicts the UV-Vis absorption change of Rh B in a given reaction time over TBA/CN-3. With prolonged reaction time, the UV-Vis absorption intensity of Rh B markedly declined, and the characteristic absorption wavelength at 552 nm shifted to 518 nm, indicating the complete disruption of the conjugated aromatic system and chromogenic groups.

Thereafter, the recycling experiments were performed to evaluate the practical applications of TBA/CN-3. As shown in Fig. 9d, it was noticeable that there was only a slight decline in the photocatalytic degradation efficiency over TBA/CN-3 after three consecutive recycles, representing excellent photostability and reusability.

To reveal the dominant oxidative species involved in the photodecomposition of Rh B, active radical capturing experiments were carried out, in which $p$-benzoquinone (BQ), isopropanol (IPA) and ammonium oxalate (AO) were introduced as the quenchers of superoxide radicals ($^{\cdot}O_2^{-}$), hydroxyl radicals ($^{\cdot}OH$) and photo-excited holes ($h^+$), respectively.[54,55] As shown in Fig. 10a, the degradation efficiency of Rh B over TBA/CN-3 significantly reduced from 92.0% to 40.5% with the addition of BQ, reduced to 47.9% with the addition of AO and slightly reduced to 75.4% with the addition of IPA. These results indicate that $^{\cdot}O_2^{-}$ and $h^+$ played the decisive roles with $^{\cdot}OH$ being partially involved in the photodegradation of Rh B. To further confirm the above-mentioned results, ESR experiments were conducted to detect the signals of $^{\cdot}O_2^{-}$ and $^{\cdot}OH$ during the photocatalytic process. It could be found from Fig. 10b and c that strong signals typical of $^{\cdot}O_2^{-}$ and $^{\cdot}OH$ were detected in TBA/CN-3, but the signals were relatively weak in CN. It signified that the TBA modification could observably benefit the yield of $^{\cdot}O_2^{-}$ and $^{\cdot}OH$ radicals in the photocatalytic degradation system.
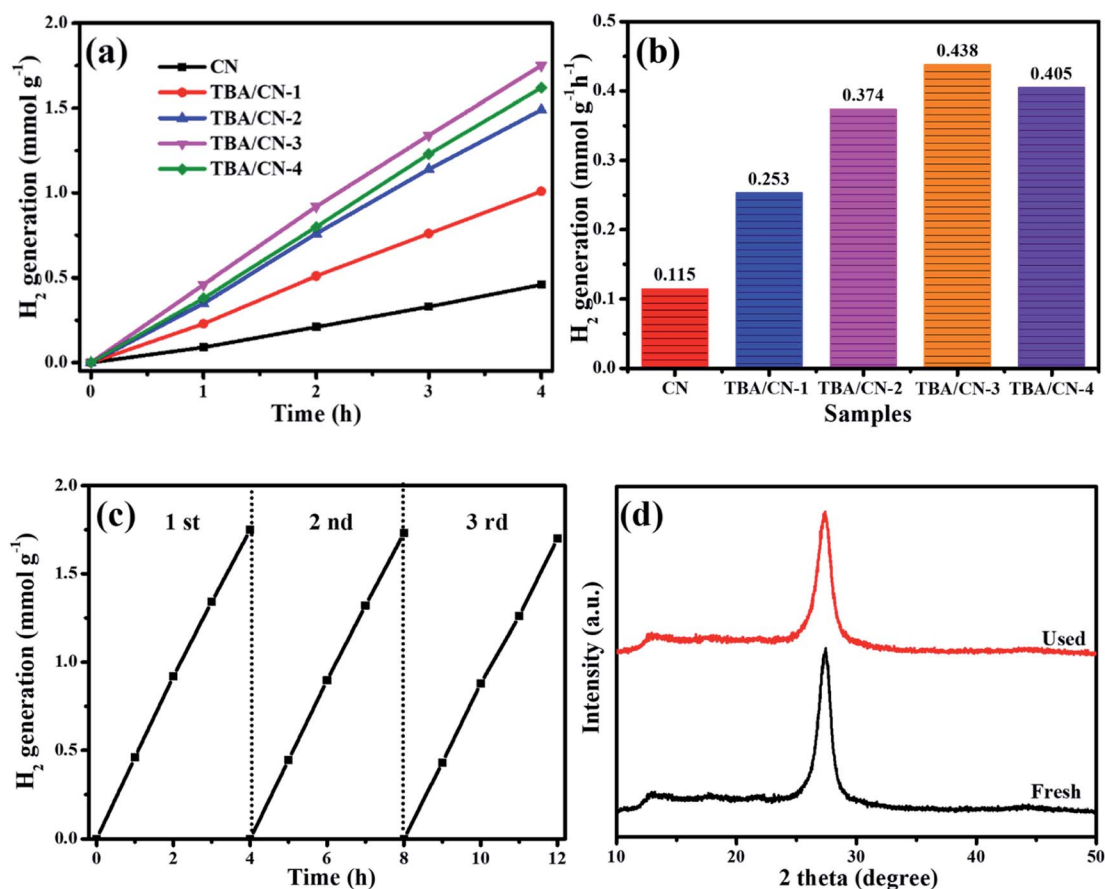


**Fig. 11** Photocatalytic $H_2$ evolution (a), corresponding $H_2$ evolution rates (b) of as-prepared samples, $H_2$ evolution cyclicity performance (c) and XRD patterns (d) of TBA/CN-3 before and after photocatalysis.

The photocatalytic $H_2$ evolution efficiency of the five as-synthesized samples was determined and the results are illustrated in Fig. 11. It can be seen in Fig. 11a that all the samples achieved stable near-linear generation of $H_2$ with marked difference in the evolution rate. The pristine CN exhibited smallest photocatalytic $H_2$ evolution rate of about 0.115 mmol $g^{-1}$ $h^{-1}$ (Fig. 11b), while the TBA/CN samples exhibited gradually enhanced rates with the increase in the concentration of the introduced TBA. The TBA/CN-3 sample possessed optimal $H_2$ evolution rate of 0.438 mmol $g^{-1}$ $h^{-1}$, which was almost 3.8 times than that of CN. The enhanced $H_2$ evolution of TBA/CN-3 was largely due to the stronger visible light harvesting and faster photo-exited charge transfer with lower recombination.

The photocatalytic $H_2$ generation experiments were also repeated three times to ensure the durability of TBA/CN-3. As shown in Fig. 11c, the TBA/CN-3 sample displayed a steady $H_2$ evolution without any apparent decline over three cycles (for 12 h in total), indicating a good photocatalytic stability and reproducibility. Furthermore, it can be seen in Fig. 11d that almost identical XRD patterns of TBA/CN-3 before and after the photocatalytic experiments further confirmed its durability.

### 3.3. Plausible mechanisms of the enhanced photocatalytic properties

In order to reveal the enhanced photocatalytic properties of TBA/CN-3, TRPL, PC value and EIS measurements were carried out. TRPL decay spectra in Fig. 12a illustrate that TBA/CN-3 presented an evident longer average lifetime of 7.44 ns compared to pure g-$C_3N_4$ (5.29 ns), suggesting the highly efficient migration of the charge carriers.[56,57] The prolonged lifetime of photo-excited charge was possibly attributable to the established unique electron transfer pathway of N–C–S–C–N (or N–C–C–C–N) *via* the introduction of TBA (Fig. 1). Thereafter, the PC value and EIS behavior of TBA/CN-3 further consolidated the observed results. As clearly depicted in Fig. 12b, the PC density of TBA/CN-3 was more robust than that of CN, suggesting dramatical enhancement of the photo-excited charge carrier migration.[58] Similarly, TBA/CN-3 exhibited a much reduced EIS Nyquist plot radius than that of pure CN, further confirming the smaller electron transfer resistance and faster charge transfer.[59]

In light of the above results, the possible mechanism of the enhanced photocatalytic Rh B degradation and $H_2$ evolution over TBA/CN composites is schematically predicted in Fig. 13. When TBA is incorporated into the skeleton of CN, extended delocalization of the lone pair electrons and unique electron transfer pathways would lead to enhanced visible light absorption, prolonged electron lifetime and facilitated charge migration. Irradiated by visible light, TBA/CN-3 was immediately activated, resulting in the production of photo-excited electrons and holes. The electrons on VB could effortlessly transfer along the bandgap to the CB of TBA/CN-3. Because of



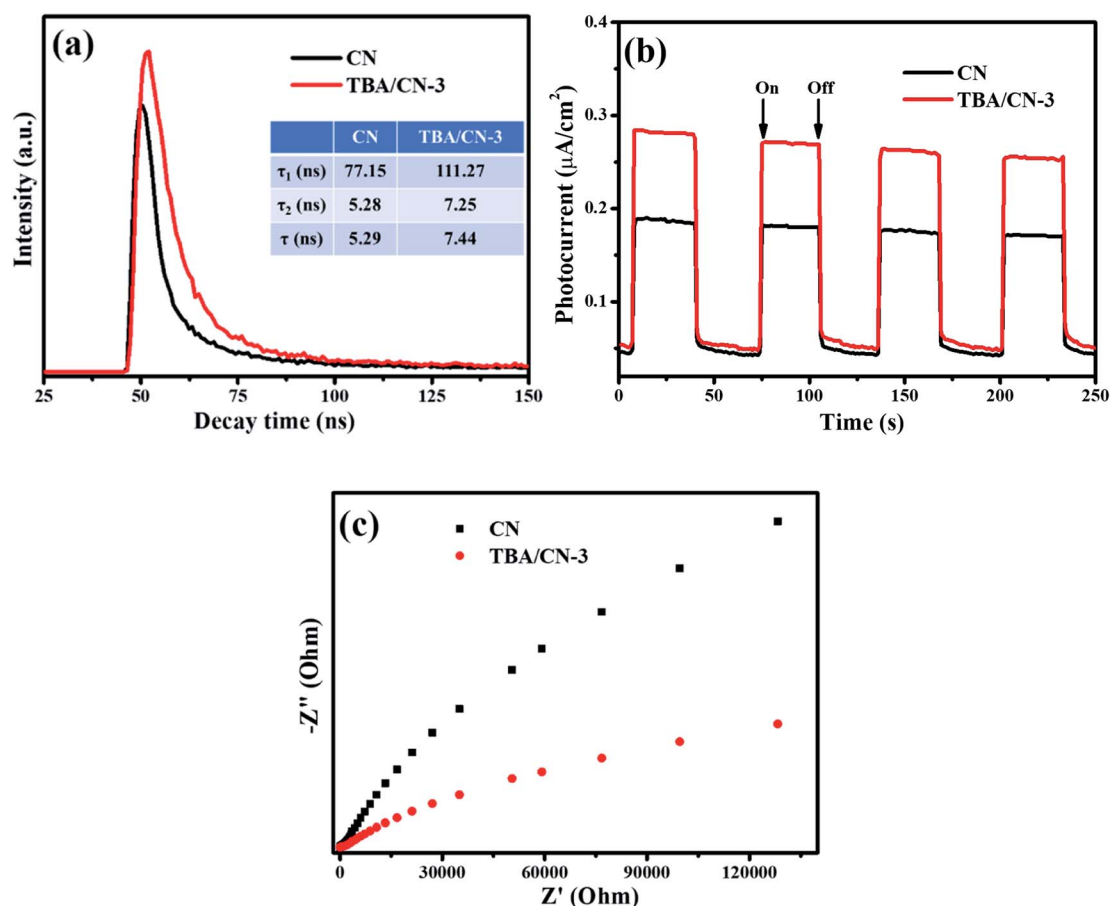| | CN | TBA/CN-3 |
|---|---|---|
| $\tau_1$ (ns) | 77.15 | 111.27 |
| $\tau_2$ (ns) | 5.28 | 7.25 |
| $\tau$ (ns) | 5.29 | 7.44 |

**Fig. 12** Comparison of the TRPL decay spectra (a), photocurrent response (b) and EIS Nyquist curves between CN and TBA/CN-3 (c).
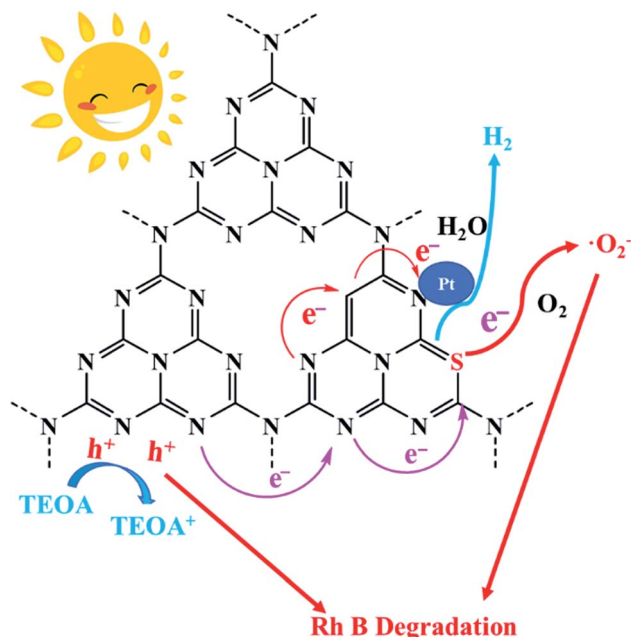
**Fig. 13** Possible mechanisms on the photocatalytic degradation of Rh B with simultaneous $H_2$ production over TBA/CN-3 under visible light irradiation.

the prolonged lifetime, the stored electrons in the CB could have more opportunities to generate $^\bullet O_2^-$ by reducing dissolved $O_2$, which was benefited from the more negative potential ($-0.86$ V $vs.$ NHE) of TBA/CN-3 than that of $O_2/^\bullet O_2^-$ ($-0.33$ V $vs.$ NHE).[60] Furthermore, these $^\bullet O_2^-$ could be further partially converted to $^\bullet OH$ through complex chain reactions. Moreover, these accumulated electrons could also easily transfer to the Pt co-catalyst and have sufficient reduction capability to product $H_2$ by water splitting on the surface of TBA/CN-3. Because of the lower VB potential ($+1.32$ V $vs.$ NHE) compared to the standard redox potential of $H_2O/^\bullet OH$ ($+1.99$ V $vs.$ NHE) and $OH^-/^\bullet OH$ ($+2.80$ V $vs.$ NHE),[61] the retained holes were not able to oxidize $H_2O$ or $OH^-$ to yield $^\bullet OH$, but could directly oxidize Rh B or react with TEOA to form $TEOA^+$. As a result, the electrons in the CB and the holes on the VB could be separated efficiently, and these holes and electrons with high strong redox capacity strongly contributed to the enhancement of the photocatalytic activity of TBA/CN-3.

## 4. Conclusion

Overall, the TBA modified g-$C_3N_4$ was synthesized by copolymerizing the mixture of urea and TBA. The systematic characterization results proved that the structural units of TBA were well incorporated into the skeleton of g-$C_3N_4$ nanosheets. The PL, TRPL and photoelectrochemical experimental results suggested that the TBA/CN samples possessed prolonged lifetime of the photo-excited carriers, enhanced carrier transfer efficiency and reduced photocurrent resistance, which were in favor of the Rh B degradation and $H_2$ evolution. The optimized TBA/CN exhibited 3.5 and 3.8-folds improved visible-light-

driven Rh B degradation and $H_2$ evolution activities compared to the pristine CN, respectively. This research may provide a new insight into the rational design of g-$C_3N_4$-based photocatalysts for efficiently visible light capture and conversion.

## Conflicts of interest

The authors declare that they have no known competing financial interests or personal relationships that could have appeared to influence the work reported in this paper.

## Acknowledgements

## References

1 H. F. Qin, Y. H. Zuo, J. T. Jin, W. L. Wang, Y. L. Xu, L. F. Cui, $et\ al.$, ZnO nanorod arrays grown on g-$C_3N_4$ micro-sheets for enhanced visible light photocatalytic $H_2$evolution, $RSC\ Adv.$, 2019, **9**, 24483–24488.

2 H. Yi, D. L. Huang, L. Qin, G. M. Zeng, C. Lai, M. Cheng, $et\ al.$, Selective prepared carbon nanomaterials for advanced photocatalytic application in environmental pollutant treatment and hydrogen production, $Appl.\ Catal.$, $B$, 2018, **239**, 408–424.

3 G. J. Guan, E. Y. Ye, M. L. You and Z. B. Li, Hybridized 2D nanomaterials toward highly efficient photocatalysis for degrading pollutants: current status and future perspectives, $Small$, 2020, **16**, 1907087.

4 N. Fajrina and M. Tahir, A critical review in strategies to improve photocatalytic water splitting towards hydrogen production, $Int.\ J.\ Hydrogen\ Energy$, 2019, **44**, 540–577.

5 C. M. Li, H. H. Wu, Y. H. Du, S. B. Xi, H. J. Dong, S. H. Wang, $et\ al.$, Mesoporous 3D/2D NiCoP/g-$C_3N_4$ Heterostructure with Dual Co-N and Ni-N Bonding States for Boosting Photocatalytic $H_2$ Production Activity and Stability, $ACS\ Sustainable\ Chem.\ Eng.$, 2020, **8**, 12934–12943.

6 K. Nakata and A. Fujishima, $TiO_2$ photocatalysis: design and applications, $J.\ Photochem.\ Photobiol.,\ C$, 2012, **13**, 169–189.

7 A. Y. Meng, L. Y. Zhang, B. Cheng and J. G. Yu, Dual Cocatalysts in $TiO_2$ Photocatalysis, $Adv.\ Mater.$, 2019, **31**, 1807660.

8 J. K. Jia, C. Y. Jiang, X. R. Zhang, P. J. Li, J. X. Xiong, Z. Zhang, $et\ al.$, Urea-modified carbon quantum dots as electron mediator decorated g-$C_3N_4$/$WO_3$ with enhanced visible-light photocatalytic activity and mechanism insight, $Appl.\ Surf.\ Sci.$, 2019, **495**, 143524.

9 J. R. Huang, X. F. Yang, S. Hussain, J. N. Tao, G. W. Liu and G. J. Qiao, Cooperative enhancement solar hydrogen

generation of reformed g-C$_3$N$_4$/TiO$_2$ mesocrystals composites, *J. Nanoelectron. Optoelectron.*, 2020, **15**, 46–53.

10 B. T. Xu, M. B. Ahmed, J. L. Zhou, A. Altaee, G. Xu and M. H. Wu, Graphitic carbon nitride based nanocomposites for the photocatalysis of organic contaminants under visible irradiation: progress, limitations and future directions, *Sci. Total Environ.*, 2018, **633**, 546–559.

11 C. Prasad, H. Tang, Q. Q. Liu, I. Bahadur, S. Karlapudi and Y. J. Jiang, A latest overview on photocatalytic application of g-C$_3$N$_4$ based nanostructured materials for hydrogen production, *Int. J. Hydrogen Energy*, 2020, **45**, 337–379.

12 S. Zhang, P. C. Gu, R. Ma, C. T. Luo, T. Wen, G. X. Zhao, *et al.*, Recent developments in fabrication and structure regulation of visible-light-driven g-C$_3$N$_4$-based photocatalysts towards water purification: a critical review, *Catal. Today*, 2019, **335**, 65–77.

13 X. Q. Xu, S. M. Wang, X. F. Yu, J. Dawa, D. L. Gui and R. H. Tang, Biosynthesis of Ag deposited phosphorus and sulfur co-doped g-C$_3$N$_4$ with enhanced photocatalytic inactivation performance under visible light, *Appl. Surf. Sci.*, 2020, **501**, 144245.

14 L. Q. Jing, Y. G. Xu, M. J. Zhou, J. J. Deng, W. Wei, M. Xie, *et al.*, Novel broad-spectrum-driven oxygen-linked band and porous defect co-modified orange carbon nitride for photodegradation of bisphenol A and 2-mercaptobenzothiazole, *J. Hazard. Mater.*, 2020, **396**, 122659.

15 X. Q. Xu, S. M. Wang, T. J. Hu, X. F. Yu, J. P. Wang and C. Jia, Fabrication of Mn/O co-doped g-C$_3$N$_4$: excellent charge separation and transfer for enhancing photocatalytic activity under visible light irradiation, *Dyes Pigm.*, 2020, **175**, 108107.

16 H. S. Li, L. L. Cai, X. Wang and H. X. Shi, Fabrication of AgCl/Ag$_3$PO$_4$/graphitic carbon nitride heterojunctions for enhanced visible light photocatalytic decomposition of methylene blue, methylparaben and *E. coli*, *RSC Adv.*, 2021, **11**, 6383–6394.

17 D. K. Chauhan, S. Jain, V. R. Battula and K. Kailasam, Organic motifs functionalization via covalent linkage in carbon nitride: an exemplification in photocatalysis, *Carbon*, 2019, **152**, 40–58.

18 Y. F. Liu, S. F. Kang, L. F. Cui and Z. Ma, Boosting near-infrared-driven photocatalytic H$_2$ evolution using protoporphyrin-sensitized g-C$_3$N$_4$, *J. Photochem. Photobiol., A*, 2020, **396**, 112517.

19 Y. A. Zhu, C. B. Xiong, S. Q. Song, Z. G. Le and S. J. Jiang, Coordination-driven synthesis of perfected π-conjugated graphitic carbon nitride with efficient charge transfer for oxygen activation and gas purification, *J. Colloid Interface Sci.*, 2019, **538**, 237–247.

20 D. Vidyasagar, S. G. Ghugal, S. S. Umare and M. Banavoth, Extended π-conjugative n-p type homostructural graphitic carbon nitride for photodegradation and charge-storage applications, *Sci. Rep.*, 2019, **9**, 7186.

21 K. L. Chen, J. Q. Yan, D. D. Sun, S. S. Zhang, Y. Y. Zhao and J. H. Huang, Electron-donating tris(p-fluorophenyl) phosphine-modified g-C$_3$N$_4$ for photocatalytic hydrogen evolution and p-chlorophenol degradation, *Int. J. Hydrogen Energy*, 2021, **46**, 1976–1988.

22 F. Y. Ge, S. Q. Huang, J. Yan, L. Q. Jing, F. Chen, M. Xie, *et al.*, Sulfur promoted n-π* electron transitions in thiophene-doped g-C$_3$N$_4$ for enhanced photocatalytic activity, *Chin. J. Catal.*, 2021, **42**, 450–459.

23 J. Liu, Y. Yu, R. L. Qi, C. Y. Cao, X. Y. Liu, Y. J. Zheng, *et al.*, Enhanced electron separation on in-plane benzene-ring doped g-C$_3$N$_4$ nanosheets for visible light photocatalytic hydrogen evolution, *Appl. Catal., B*, 2019, **244**, 459–464.

24 W. Yang, X. Y. Shan, Y. Chen and Y. H. Gao, Enhanced photocatalytic performance of C$_3$N$_4$ via doping with π-deficient conjugated pyridine ring and BiOCl composite heterogeneous materials, *Diamond Relat. Mater.*, 2020, **108**, 107926.

25 C. Y. Zhou, D. L. Huang, P. Xu, G. M. Zeng, J. H. Huang, T. Z. Shi, *et al.*, Efficient visible light driven degradation of sulfamethazine and tetracycline by salicylic acid modified polymeric carbon nitride via charge transfer, *Chem. Eng. J.*, 2019, **370**, 1077–1086.

26 X. Y. Wei, X. P. Xu, X. F. Yang, J. Y. Li and Z. G. Liu, Visible light degradation of reactive black-42 by novel Sr/Ag-TiO$_2$@g-C$_3$N$_4$ photocatalyst: RSM optimization, reaction kinetics and pathways, *Spectrochim. Acta, Part A*, 2020, **228**, 117870.

27 J. R. Bai, P. Zhou, P. Xu, Y. Y. Deng and Q. F. Zhou, Synergy of dopants and porous structures in graphitic carbon nitride for efficient photocatalytic H$_2$ evolution, *Ceram. Int.*, 2021, **47**, 4043–4048.

28 P. She, J. Li, H. G. Bao, X. Q. Xu and Z. Hong, Green synthesis of Ag nanoparticles decorated phosphorus doped g-C$_3$N$_4$ with enhanced visible-light-driven bactericidal activity, *J. Photochem. Photobiol., A*, 2019, **384**, 112028.

29 H. Y. Ji, Y. M. Fan, J. Yan, Y. G. Xu, X. J. She, J. M. Gu, *et al.*, Construction of SnO$_2$/graphene-like g-C$_3$N$_4$ with enhanced visible light photocatalytic activity, *RSC Adv.*, 2017, **7**, 36101–36111.

30 T. T. Zhu, Y. H. Song, H. Y. Ji, Y. G. Xu, Y. X. Song, J. X. Xia, *et al.*, Synthesis of g-C$_3$N$_4$/Ag$_3$VO$_4$ composites with enhanced photocatalytic activity under visible light irradiation, *Chem. Eng. J.*, 2015, **271**, 96–105.

31 G. R. Jia, Y. Wang, X. Q. Cui, Z. X. Yang, L. L. Liu, H. Y. Zhang, *et al.*, Asymmetric embedded benzene ring enhances charge transfer of carbon nitride for photocatalytic hydrogen generation, *Appl. Catal., B*, 2019, **258**, 117959.

32 Z. Zhu, P. W. Huo, Z. Y. Lu, Y. S. Yan, Z. Liu, W. D. Shi, *et al.*, Fabrication of magnetically recoverable photocatalysts using g-C$_3$N$_4$ for effective separation of charge carriers through like-Z-scheme mechanism with Fe$_3$O$_4$ mediator, *Chem. Eng. J.*, 2018, **331**, 615–625.

33 Q. Liang, M. Zhang, C. H. Liu, S. Xu and Z. Y. Li, Sulfur-doped graphitic carbon nitride decorated with zinc phthalocyanines towards highly stable and efficient photocatalysis, *Appl. Catal., A*, 2016, **519**, 107–115.

34 J. R. Bai, C. C. Yin, H. Y. Xu, G. Chen, Z. J. Ni, Z. L. Wang, *et al.*, Facile urea-assisted precursor pre-treatment to

fabricate porous g-C₃N₄ nanosheets for remarkably enhanced visible-light-driven hydrogen evolution, *J. Colloid Interface Sci.*, 2018, **532**, 280–286.

35 M. Y. Ding, W. Wang, Y. J. Zhou, C. H. Lu, Y. R. Ni and Z. Z. Xu, Facile in situ synthesis of 2D porous g-C₃N₄ and g-C₃N₄/P25(N) heterojunction with enhanced quantum effect for efficient photocatalytic application, *J. Alloys Compd.*, 2015, **635**, 34–40.

36 G. M. Ba, T. T. Huo, Q. H. Deng, H. P. Li and W. G. Hou, Mechanochemical synthesis of nitrogen-deficient mesopore-rich polymeric carbon nitride with highly enhanced photocatalytic performance, *ACS Sustainable Chem. Eng.*, 2020, **8**, 18606–18615.

37 L. Shi, L. Q. Yang, W. Zhou, Y. Y. Liu, L. S. Yin, X. Hai, *et al.*, Photoassisted construction of holey defective g-C₃N₄ photocatalysts for efficient visible-light-driven H₂O₂ production, *Small*, 2018, **14**, 1703142.

38 Y. J. Zhou, J. Z. Li, C. Y. Liu, P. W. Huo and H. Q. Wang, Construction of 3D porous g-C₃N₄/AgBr/rGO composite for excellent visible light photocatalytic activity, *Appl. Surf. Sci.*, 2018, **458**, 586–596.

39 H. Tang, R. Wang, C. X. Zhao, Z. P. Chen, X. F. Yang, D. Bukhvalov, *et al.*, Oxamide-modified g-C₃N₄ nanostructures: tailoring surface topography for high-performance visible light photocatalysis, *Chem. Eng. J.*, 2019, **374**, 1064–1075.

40 H. P. Li, Z. W. Liang, Q. H. Deng and W. G. Hou, Band structure engineering of polymeric carbon nitride with oxygen/carbon codoping for efficient charge separation and photocatalytic performance, *J. Colloid Interface Sci.*, 2020, **564**, 333–343.

41 H. N. Che, C. X. Li, P. J. Zhou, C. B. Liu, H. J. Dong and C. M. Li, Band structure engineering and efficient injection rich-pi-electrons into ultrathin g-C₃N₄ for boosting photocatalytic H₂ production, *Appl. Surf. Sci.*, 2020, **505**, 144564.

42 Y. C. Lu, J. Chen, A. J. Wang, N. Bao, J. J. Feng, W. P. Wang, *et al.*, Facile synthesis of oxygen and sulfur co-doped graphitic carbon nitride fluorescent quantum dots and their application for mercury(II) detection and bioimaging, *J. Mater. Chem. C*, 2015, **3**, 73–78.

43 H. Q. Lv, Y. Huang, R. T. Koodali, G. M. Liu, Y. B. Zeng, Q. G. Meng, *et al.*, Synthesis of sulfur-doped 2D graphitic carbon nitride nanosheets for efficient photocatalytic degradation of phenol and hydrogen evolution, *ACS Appl. Mater. Interfaces*, 2020, **12**, 12656–12667.

44 C. C. Hu, W. Z. Hung, M. S. Wang and P. J. Lu, Phosphorus and sulfur codoped g-C₃N₄ as an efficient metal-free photocatalyst, *Carbon*, 2018, **127**, 374–383.

45 Z. Chen, T. T. Fan, M. Y. Shao, X. Yu, Q. L. Wu, J. H. Li, *et al.*, Simultaneously enhanced photon absorption and charge transport on a distorted graphitic carbon nitride toward visible light photocatalytic activity, *Appl. Catal., B*, 2019, **242**, 40–50.

46 Y. Z. Hong, C. S. Li, G. Y. Zhang, Y. D. Meng, B. X. Yin, Y. Zhao, *et al.*, Efficient and stable Nb₂O₅ modified g-C₃N₄

photocatalyst for removal of antibiotic pollutant, *Chem. Eng. J.*, 2016, **299**, 74–84.

47 Y. Z. Hong, Z. Y. Fang, B. X. Yin, B. F. Luo, Y. Zhao, W. D. Shi, *et al.*, A visible-light-driven heterojunction for enhanced photocatalytic water splitting over Ta₂O₅ modified g-C₃N₄ photocatalyst, *Int. J. Hydrogen Energy*, 2017, **42**, 6738–6745.

48 L. Ge, C. C. Han, X. L. Xiao, L. L. Guo and Y. J. Li, Enhanced visible light photocatalytic hydrogen evolution of sulfur-doped polymeric g-C₃N₄ photocatalysts, *Mater. Res. Bull.*, 2013, **48**, 3919–3925.

49 Y. Q. Yang, H. F. Jin, C. Zhang, H. H. Gan, F. T. Yi and H. Q. Wang, Nitrogen-deficient modified P-Cl co-doped graphitic carbon nitride with enhanced photocatalytic performance, *J. Alloys Compd.*, 2020, **821**, 153439.

50 Y. W. Yuan, L. L. Zhang, J. Xing, M. I. B. Utama, X. Lu, K. Z. Du, *et al.*, High-yield synthesis and optical properties of g-C₃N₄, *Nanoscale*, 2015, **7**, 12343–12350.

51 P. Y. Lin, J. Shen, X. H. Yu, Q. Q. Liu, D. S. Li and H. Tang, Construction of Ti₃C₂ MXene/O-doped g-C₃N₄ 2D-2D Schottky-junction for enhanced photocatalytic hydrogen evolution, *Ceram. Int.*, 2019, **45**, 24656–24663.

52 G. Q. Zhang, Y. S. Xu, C. X. He, P. X. Zhang and H. M. Mi, Oxygen-doped crystalline carbon nitride with greatly extended visible-light-responsive range for photocatalytic H₂ generation, *Appl. Catal., B*, 2021, **283**, 119636.

53 F. Li, P. Zhu, S. M. Wang, X. Q. Xu, Z. J. Zhou and C. D. Wu, One-pot construction of Cu and O co-doped porous g-C₃N₄ with enhanced photocatalytic performance towards the degradation of levofloxacin, *RSC Adv.*, 2019, **9**, 20633–20642.

54 Y. Z. Hong, C. S. Li, B. X. Yin, D. Li, Z. Y. Zhang, B. D. Mao, *et al.*, Promoting visible-light-induced photocatalytic degradation of tetracycline by an efficient and stable beta-Bi₂O₃@g-C₃N₄ core/shell nanocomposite, *Chem. Eng. J.*, 2018, **338**, 137–146.

55 D. Li, F. F. Shi, D. L. Jiang, M. Chen and W. D. Shi, CdIn₂S₄/g-C₃N₄ heterojunction photocatalysts: enhanced photocatalytic performance and charge transfer mechanism, *RSC Adv.*, 2017, **7**, 231–237.

56 Y. X. Wang, L. Rao, P. F. Wang, Y. Guo, X. Guo and L. X. Zhang, Porous oxygen-doped carbon nitride: supramolecular preassembly technology and photocatalytic degradation of organic pollutants under low-intensity light irradiation, *Environ. Sci. Pollut. Res.*, 2019, **26**, 15710–15723.

57 L. Luo, J. N. Ma, H. X. Zhu and J. W. Tang, Embedded carbon in a carbon nitride hollow sphere for enhanced charge separation and photocatalytic water splitting, *Nanoscale*, 2020, **12**, 7339–7346.

58 T. J. Chen, C. J. Song, M. S. Fan, Y. Z. Hong, B. Hu, L. B. Yu, *et al.*, In situ fabrication of CuS/g-C₃N₄ nanocomposites with enhanced photocatalytic H₂ production activity via photoinduced interfacial charge transfer, *Int. J. Hydrogen Energy*, 2017, **42**, 12210–12219.

59 Q. Y. Chen, H. L. Dou, S. H. Zheng, X. Rao and Y. P. Zhang, Photocatalytic H₂ evolution and MB degradation over nickel-doped graphitic carbon nitride microwires under visible light irradiation, *J. Photochem. Photobiol., A*, 2019, **382**, 111931.

60 T. Y. Wang, W. Quan, D. L. Jiang, L. L. Chen, D. Li, S. C. Meng, *et al.*, Synthesis of redox-mediator-free direct Z-scheme AgI/WO$_3$ nanocomposite photocatalysts for the degradation of tetracycline with enhanced photocatalytic activity, *Chem. Eng. J.*, 2016, **300**, 280–290.

61 H. Guo, N. Jiang, H. J. Wang, N. Lu, K. F. Shang, J. Li, *et al.*, Degradation of antibiotic chloramphenicol in water by pulsed discharge plasma combined with TiO$_2$/WO$_3$ composites: mechanism and degradation pathway, *J. Hazard. Mater.*, 2019, **371**, 666–676.